

SEARCH FOR HIGH-MASS PROTOSTELLAR OBJECTS IN COLD IRAS SOURCES

Y. AO,^{1,2} J. YANG,¹ K. TATEMATSU,² C. HENKEL,^{3,4} K. SUNADA,⁵ AND Q. NGUYEN-LUONG^{2,6}

¹*Purple Mountain Observatory & Key Laboratory for Radio Astronomy, Chinese Academy of Sciences, 8 Yuanhua Road, Nanjing 210034, China*

²*National Astronomical Observatory of Japan, 2-21-1 Osawa, Mitaka, Tokyo 181-8588, Japan*

³*MPIfR, Auf dem Hügel 69, 53121 Bonn, Germany*

⁴*Astron. Dept., King Abdulaziz Univ., P.O. Box 80203, Jeddah 21589, Saudi Arabia*

⁵*Mizusawa VLBI Observatory, NAOJ, 2-12 Hoshi-ga-oka, Mizusawa-ku, Oshu-shi, Iwate 023-0861, Japan*

⁶*Korea Astronomy and Space Science Institute, 776 Daedeokdae-ro, Yuseong-gu, Daejeon 34055, Korea*

ABSTRACT

We present the results of CS $J=2\rightarrow 1$ mapping observations towards 39 massive star forming regions selected from the previous CO line survey of cold IRAS sources with high-velocity CO flows along the Galactic plane (Yang et al. 2002). All sources are detected in CS $J=2\rightarrow 1$, showing the existence of CS clumps around the IRAS sources. However, one third of the sources are not deeply embedded in the dense clumps by comparison of the central powering IRAS sources and the morphologies of CS clumps. Physical parameters of the dense molecular clumps are presented. We have identified 12 high-mass protostellar object (HMPO) candidates by checking the association between the dense cores and the IRAS sources, the detection of water maser, and the radio properties towards the IRAS sources. We find that the HMPO sources are characterized by low FIR luminosity to virial mass ratios since they are in very early evolutionary stages when the massive protostars have not reached their full luminosities, which are typical for zero-age main sequence stars. Large turbulent motion in the HMPO sources may be largely due to the large kinetic energy ejected by the central protostars formed in the dense clumps. However, alternative means or undetected outflows may also be responsible for the turbulence in the clumps.

Keywords: ISM:clouds — ISM:molecules — stars:formation — stars:massive — stars: protostars

1. INTRODUCTION

In recent years, more attention has been paid to the study of massive star formation (MSF), due to their predominant role in the evolution of the interstellar medium and the Galaxy. To study the physical properties, especially the initial conditions, of MSF, it is very important to search for high-mass protostellar objects (HMPOs) before the energetic processes such as powerful jets, outflows and strong ultraviolet (UV) radiation destroy their natal clouds in the massive star forming regions (MSFRs). HMPOs are usually formed in clusters and tend to be deeply embedded in the gas clouds. At the early stage of MSF, a HMPO can not produce a detectable H II region, even though the central protostar produces a lot of UV photons, because these photons can not travel far from the protostar before being absorbed by the surrounding material and the size of the ionized gas region is extremely small, making it undetectable at centimeter wavelengths with current sensitivities (Churchwell 2002). Therefore, HMPOs are characterized by high infrared luminosity, strong dust emission and very weak or no detectable free-free emission at centimeter wavelengths (Garay & Lizano 1999; Hosokawa & Omukai 2009; Hosokawa et al. 2010). As a consequence, large surveys aiming at characterizing the physical properties of MSFRs and searching for embedded massive young stellar objects (YSOs) have been made using high-density tracers, e.g., CS, HCO⁺, or HCN, and submillimeter dust continuum emission (Plume et al. 1992, 1997; Zinchenko et al. 1994, 1995, 1998; Bronfman et al. 1996; Juvela 1996; Molinari et al. 1998a; Cesaroni et al. 1999; Hunter et al. 2000; Brand et al. 2001; Sridharan et al. 2002; Beuther et al. 2002a; Shirley et al. 2003; Ao et al. 2004; Faúndez et al. 2004; Williams et al. 2004; Fontani et al. 2005; Klein et al. 2005; Schnee & Carpenter 2009; Elia et al. 2017). In particular, the Red MSX Source (RMS) survey is a large MSX-selected sample with multiwavelength data (Urquhart et al. 2007a,b, 2008, 2009a,b, 2011a,b, 2012, 2014a, 2015; Mottram et al. 2007, 2010, 2011; Cooper et al. 2013; Lumsden et al. 2013; Maud et al. 2015a,b). The APEX Telescope Large Area Survey of the Galaxy (ATLASGAL) survey (Schuller et al. 2009) is the first unbiased continuum survey of the whole inner Galactic disk at 870 μ m (Tackenberg et al. 2012; Wienen et al. 2012, 2015; Urquhart et al. 2013a,b, 2014b; Csengeri et al. 2016a,b, 2017; Li et al. 2016; Giannetti et al. 2017; Tang et al. 2018; Yang et al. 2018). Both RMS and ATLASGAL surveys are ideal samples for identifying YSOs and are useful in comparison with other studies.

The search for HMPOs in the Milky Way was often based on source catalogs from the unbiased all-sky infrared surveys and color-color selection criteria (Wood & Churchwell 1989, Yang et al. 2002). Further removal of contamination induced by color-color selection is conducted by detecting dense gas tracers such as CS, HCO⁺, and HCN and early-stage star formation activity such as masers in the HMPO candidates (Beuther et al. 2002a; Wu et al. 2010). While the new all-sky infrared compact source catalog from the Planck mission is available now (Planck Consortium et al. 2016), the older all-sky infrared source catalog from IRAS satellite is still a good foundation to search for HMPOs in the Milky Way as the peaks of the HMPOs spectral energy distribution is at the IRAS wavebands of 60–100 μ m (Sridharan et al. 2002). Yang et al. (2002) applied cold-color selection criteria to the IRAS source catalog to search for CO in 1912 cold IRAS sources belonging to the northern Galactic plane. 1331 of these sources were detected. In that paper, they also identified 289 high-velocity CO flows (HVF) on the basis of the existence of broad CO line wing emission. Among these HVFs, 151 sources have an infrared (IR) luminosity $> 10^3 L_{\odot}$ and are thought to be a good target sample of early stage MSFRs. Although the central massive stars have been formed around these IRAS sources, the natal molecular clouds must still exist and can provide essential clues for ongoing or incipient massive star formation. In this paper, we conduct a search for HMPOs by randomly selecting 39 out of the 151 luminous HVFs (Yang et al. 2002) and perform CS $J=2\rightarrow 1$ mapping with the Nobeyama 45m radio telescope. It is an extension of our previous work on the CS $J=2\rightarrow 1$ study of 10 IRAS sources (Ao et al. 2004). We describe the observations in Section 2. The observational results and the HMPOs candidates are discussed in Section 3. In Section 4, we discuss the physical properties of the HMPO sample focusing on the luminosity to mass ratio and its implication to massive star formation. Finally, we provide our conclusion in Section 5.

2. OBSERVATIONS

Observations were carried out with the 45m telescope of the Nobeyama Radio Observatory (NRO) in 2004 February 21 to 23 and 2005 May 21 to 23. The receiver front end was the 25 BEams Array Receiver System (BEARS) (Sunada et al. 2000). The half-power beam width of the NRO 45m telescope was approximately 17'' for the CS $J=2\rightarrow 1$ observations. The double sideband system temperature was around 200-400 K, depending on weather conditions and different beams of the BEARS. The main beam efficiency was about 0.52 at 100 GHz and the velocity resolution was about 0.1 km s⁻¹.

The observations were performed in a snapshot mode. Since the beam separation of the BEARS was $41.1''$, four snapshots were observed to reduce the grid spacing to one half of the beam separation, i.e. $20.5''$, which is slightly larger than the beam size of $17''$. Figure 1 shows the mapping positions and profile map towards one source, IRAS 02232+6138. Spectra marked by a cross symbol with the specific color were taken from one snapshot observation, providing 25 spectra by the BEARS simultaneously, and in total 100 spectra were obtained. 10×10 mapping observations were carried out for most sources except for 04324+5106, 05375+3540, 18592+0108, 22543+6145 and 23140+6121. The mapping area of the latter five sources were extended to cover the whole emission regions. The typical on-source time was about 10 to 20 minutes for one source. To obtain the scaling factor of each beam of the BEARS, the calibrator S140 was observed with the BEARS and a single-sideband SIS receiver S100. The r.m.s. noise temperature on a main beam brightness temperature scale was about 0.6 K at a velocity resolution of 0.1 km s^{-1} . The pointing was checked by nearby SiO masers around the target every two hours and the pointing accuracy was within $5''$.

The source list is given in Table 1. We give the IR luminosity of associated IRAS point source calculated as in Casoli et al. (1986). The results derived from the IRAS data are also presented in Table 1.

3. RESULTS

3.1. Determining the distances of IRAS sources

Distances were obtained from extensive literature search. For 10 sources, we adopt their parallax measurements (for details see Table 1). We take photometric distances for 16 sources associated with OB associations and H II regions when available. For the remaining 13 sources, we calculate kinematic distances using the revised prescription given in Reid et al. (2009). Of these, IRAS 18567+0700, IRAS 20216+4107 and IRAS 20220+3728 have distance ambiguity.

IRAS 18567+0700: If we adopt its far kinematic distance of 10.8 kpc, its infrared luminosity will be $\sim 1.4 \times 10^5 L_{\odot}$ and should be detectable at radio. However, it was not detected at 1.4 GHz with a 5σ upper limit of 2.5 mJy. Thus, we adopt its near kinematic distance of 2.1 kpc.

IRAS 20216+4107: The source is associated with Cygnus X complex, thus we adopt its far kinematic distance of 2.3 kpc.

IRAS 20220+3728: If we adopt the near kinematic distance of 0.33 kpc, its infrared luminosity will be $\sim 3.2 \times 10^2 L_{\odot}$ and the source is unlikely to produce a detectable H II region. However, this source is detected with a radio flux of 0.63 Jy at 1.4 GHz. Thus, we adopt its far kinematic distance of 3.7 kpc.

The typical uncertainties of the adopted distances are about 10 to 20%. For example, the after-mentioned $L_{\text{IR}}/M_{\text{VIR}}$ ratio in § 4.1 is directly proportional to the distance. The variance at a level of 10 to 20% will not change our analysis and conclusions in the following.

3.2. CS $J=2 \rightarrow 1$ results

CS $J=2 \rightarrow 1$ emission has been detected towards all sources, showing the existence of CS clumps around the IRAS sources. Figure 2 shows the spectra of the peak positions of CS clumps close to the IRAS sources. A few targets show double peaked line profiles. IRAS 02459+6029 and IRAS 23030+5958 have two distinct velocity components, which are associated with two distinct clumps. Another two sources, IRAS 02232+6138 and IRAS 23385+6053, with blue-skewed profiles may be caused by infalling motion of gas. The results, including integrated intensities and positions of the peak spectra of the clumps, are presented in Table 2. The peak intensities of the sources cover a range from 1.64 K to 16.65 K, and the median and averaged values are 4.14 K and 5.16 K, respectively.

Contour maps of CS $J=2 \rightarrow 1$ integrated intensity are shown in Figure 3. The typical mapping sizes are $200'' \times 200''$, but for IRAS 04324+5106, 05375+3540, 18592+0108, 22543+6145 and 23140+6121, larger maps are obtained to cover the whole emission regions. Physical parameters of the clumps, such as radius R , averaged line width $\overline{\Delta v}$ and virial mass M_{VIR} , are calculated in the following ways. The angular extent of each source is determined by finding the area within the half-power contour, $A_{1/2}$ and calculating the angular size of a circle with the same area. The nominal radius, R , is determined by deconvolving the telescope beam, θ_{MB} , via the formula $R = D(\frac{A_{1/2}}{\pi} - \frac{\theta_{\text{MB}}^2}{4})^{1/2}$, where D is the distance to the source. The virial mass for a homogeneous spherical clump, neglecting contributions from the magnetic field and surface pressure, can be calculated from the expression $M_{\text{VIR}}(M_{\odot}) = 0.509 D(\text{kpc}) \theta(\text{arcsec}) \overline{\Delta v}^2$ where θ is the deconvolved angular size and $\overline{\Delta v}$ is the mean line width of a positions within the CS $J=2 \rightarrow 1$ half-power contour. The results are presented in Table 3. Clump radius, averaged line width and virial mass are given in Column 2-4. The typical radial size in the sample is 0.33 pc, ranging from 0.15 pc to 1.66 pc. The median values for the averaged line width $\overline{\Delta v}$ and virial mass M_{VIR} are 2.28 km s^{-1} and $360 M_{\odot}$, respectively.

3.3. HMPO candidates

To study the initial conditions of MSFRs at the early stage, we will identify a sample of HMPO candidates by checking the association between the dense cores and the IRAS sources, the detection of water masers, and the radio properties towards the IRAS sources.

3.3.1. Association between dense clumps and the IRAS sources

Our sample is selected from IRAS sources with large far-infrared (FIR) luminosities and broad CO line wing emission. Large luminosities suggest massive young stars have been formed or are being formed at the sites of the IRAS sources. The broad CO wing emission is likely caused by strong winds/outflows from IRAS sources, suggesting the objects are still in an early evolutionary stage. Thus our sample tends to define a collection of sources in an early evolutionary stage. However, a few of these sources may already be more evolved, where strong feedbacks have destroyed most of their natal molecular clumps. To search for the HMPOs in the early stage, we should exclude such sources by checking whether the IRAS sources are still deeply embedded in their molecular dense clumps.

If an IRAS source is located within the CS $J=2\rightarrow1$ half-power contour, we classify it as an embedded source within the dense molecular clump. In total, there are 26 sources embedded in the dense gas clouds while the remaining 13 sources are offset from the dense gas peak (see Figure 3 and Column 6 of Table 3).

3.3.2. Radio continuum emission

We used the radio data from the NRAO VLA Sky Survey (Condon et al. 1998), which is a 1.4 GHz continuum survey covering the entire sky north of -40 deg declination. We searched for the radio emission within $30''$ of the positions of the IRAS sources and their integrated flux densities are given in Table 4. For undetected sources, an upper 3σ limit is given. Then we calculate the geometry-independent parameters (the excitation parameters and the Lyman continuum photon fluxes) as in Kurtz et al. (1994). The results are summarized in Table 4. Radio spectral types of the stars (Panagia 1973) required to produce the Lyman continuum photon fluxes, N'_c , of the sources are given in column 7 of Table 4.

From the IR luminosity, one can estimate a stellar spectral type under the assumption that the entire IR emission is due to a single star (Panagia 1973). However, the single-star assumption could be too simple and not appropriate, and we should assume that an IRAS source is the site where a star cluster is formed. Therefore we adopt the universal initial mass function (IMF) of the stars following Kroupa (2001) and the mass-luminosity relationship of the zero age main sequence stars (Schaller et al. 1992). Then we can estimate the most massive stars formed in the clusters with the comparable infrared luminosities as the IRAS sources. The estimated IR spectral types of the most massive stars are presented in Column 4 of Table 4. We consider that a source can not be a good HMPO candidate when its IR spectral type is later than the radio spectral type derived as above and the difference between both spectral types is more than one spectral type. This criterion will select the sources without much evolved H II regions compared to their FIR luminosities. This criterion will exclude 22475+5939 and 23030+5958 as good HMPO candidates even if they satisfy other criteria. The results are summarized in Table 4.

3.3.3. Water masers

In star-forming regions, water maser emission at 22 GHz is often associated with high mass YSOs (Elitzur et al. 1989) and believed to be one of the best tracers to investigate the earliest phases of star formation. Interferometric observations suggest that water masers are associated with jets or winds near the base of the outflows (Torrelles et al. 2003; Goddi et al. 2005; Moscadelli et al. 2005). All sources in our sample have been observed to search for water masers (Sunada et al. 2007). The results are given in Table 4. Water masers are detected towards 25 out of 39 sources. This detection rate is much higher than that of the whole sample of cold IRAS sources in Sunada et al. (2007) where 222 out of 1563 sources was detected with maser emission, and further higher than those in another two large surveys by Wouterloot et al. (1993) and Palumbo et al. (1994). The detection rate of water masers can be explained in a framework of the evolutionary sequence of MSF (Schnee & Carpenter 2009): at an early stage, the H II regions are gravitationally bound to the protostars and remain compact in size and can not be detected at centimeter wavelength with current sensitivities; as protostars grow and become massive enough to produce detectable H II regions that can not be suppressed by the stellar gravitational potential (Keto 2007); and then the H II regions expand and destroy the accretion disks and vast parts of the ambient cloud, which are thought to be the source of water masers and outflows. Water masers have not been found towards 14 out of 39 IRAS sources and these sources may not be good HMPO candidates (see Table 4).

3.3.4. HMPO candidates identified in this sample

An IRAS source is thought to contain a star cluster instead of a single star. By adopting the universal initial mass function (IMF) of the stars following Kroupa (2001) and the mass-luminosity relationship of the zero age main sequence stars (Schaller et al. 1992), the mass of the most massive star formed in the cluster is $8 M_{\odot}$ if the FIR luminosity of an IRAS source is $\sim 8 \times 10^3 L_{\odot}$. Table 4 presents the final HMPO sample carefully identified after checking association between dense clumps and IRAS sources in § 3.3.1, the radio properties in § 3.3.2, and the existence of water masers in § 3.3.3. In total, we have identified 12 HMPO candidates in 27 sources with luminosities above $8 \times 10^3 L_{\odot}$.

3.3.5. Subgroups in the sample

To better investigate the physical conditions of MSFRs, we divided the 39 sources into five subgroups based on their luminosities and identified HMPO candidates as below: 1. subgroup **Low** with luminosities less than $8 \times 10^3 L_{\odot}$ and the mass of the most massive star formed in the cluster is less than $8 M_{\odot}$; 2. subgroup **HMPO** identified in § 3.3.4, with a FIR luminosity ranging from 8×10^3 to $1 \times 10^5 L_{\odot}$; 3. subgroup **Control** contains the remaining sources in the same FIR luminosity range as subgroup **HMPO**; 4. subgroup **Extreme** with FIR luminosities over $1 \times 10^5 L_{\odot}$; and 5. Subgroup **High** contains the **HMPO**, **Control** and **Extreme** sources with FIR luminosities over $8.0 \times 10^3 L_{\odot}$.

We compute the dynamical timescale, free-fall timescale, star formation timescale and kinetic energy for the sample and list their median values for each subgroup in Table 5. A dynamical timescale, t_{dyn} , is defined as $t_{\text{dyn}} = 2R/v$, where R is the radius of molecular clump and v the velocity. Observed line width and velocity dispersion can be related to one dimensional velocity dispersion via $\sigma_v = \Delta V/2.355$ (Pan & Padoan 2009) and $v^2 = 3\sigma_v^2$. A free-fall timescale, t_{ff} , can be obtained by $t_{\text{ff}} = \sqrt{\frac{3\pi}{32G\rho}}$, where G is the gravitational constant and ρ the gas density determined by the virial gas mass and radius of a molecular clump. A star formation timescale is estimated by adopting a turbulent core model for massive star formation (McKee & Tan 2003). We calculate the kinetic energy of a molecular clump by $E_{\text{kin}} = \frac{1}{2}M_{\text{VIR}}v^2$. These three timescales are typically a few 10^5 yrs and the kinetic energies range from 3.1×10^{45} to 6.9×10^{46} ergs.

3.4. Comments on individual HMPO candidates

Here we briefly describe the HMPO candidates with detailed information in the literatures.

3.4.1. IRAS 02232+6138

In Fig. 3, we present the CS $J=2 \rightarrow 1$ integrated intensity map. The CS centroid clearly differ from the IRAS source with a large offset of $\sim 20''$. Two outflows, with well separated bipolar lobes, are obviously detected with an offset of $\sim 25''$ from the IRAS source (Zapata et al. 2011). They are close to the CS centroid where the most blue-skewed spectrum is detected (Fig. 1), showing the distinct signature of infalling motion (Wu & Evans 2003). The hot molecular core (HMC) of W3(OH) in IRAS 02232+6138 was well studied by Wyrowski et al. (1997, 1999), and it coincides with the CS centroid and the location with the most blue-skewed spectrum.

3.4.2. IRAS 02575+6017

IRAS 02575+6017 is the eastern part of the W5-East H II region, which is the eastern part of the W5 H II region (Carpenter et al. 2000; Niwa et al. 2009). Bright-rimmed clouds in the W5-East H II region (Niwa et al. 2009) are well studied to investigate the triggered star formation caused by UV radiation from the central exciting star. The dense gas around IRAS 02575+6017 is compressed by the UV radiation or stellar wind from the exciting star in the W5-East H II region, which results in that the dense cloud has a head-tail structure, as shown in Fig. 3.

3.4.3. IRAS 06099+1800

This region is a part of the S254-258 complex as a group of five H II regions. Most studies in the complex focus on the region around IRAS 06099+1800, S255IR and the region, S255N, $1'$ north of S255IR (Miralles et al. 1997; Minier et al. 2005; Cyganowski et al. 2007; Klaassen & Wilson 2007; Chavarría et al. 2008). The former has a young massive star cluster, and the latter is associated with signposts of massive star formation at an early stage since no near infrared source is associated with it. Cyganowski et al. (2007) showed evidence of a massive protocluster in S255N. They found three cores at 1.3 mm with no IR counterpart, with masses between 6 and $35 M_{\odot}$.

In Fig. 3, we present the CS $J=2 \rightarrow 1$ integrated intensity map around IRAS 06099+1800 and reveal that the IRAS source is deeply embedded in the center of the dense gas cloud, which is elongated from north to south-east. CS $J=2 \rightarrow 1$

emission (see Fig. 3) peaks at S255IR and elongated towards S255N, but $\text{N}_2\text{H}^+(1-0)$ peaks at S255N (Pirogov et al. 2003). Klaassen & Wilson (2007) found the signatures of infall towards S255IR and S255N. Both of the regions are HMPO candidates, but S255N is at the earlier stage.

3.4.4. IRAS 22543+6145

In Fig. 3, we present the CS integrated intensity map and the 3.6 cm VLA map around IRAS 22543+6145. The dense gas is elongated from north to south, and two dense molecular clumps are revealed, one is associated with the IRAS source and another one is $140''$ south of the IRAS source. Many authors (e.g., Narayanan et al. 1996; Wu et al. 2005; Xu et al. 2006b) have found the bipolar outflow towards this region. Wu & Evans (2003) and Klaassen & Wilson (2007) found the signature of infall, which suggests that the IRAS source could be a HMPO.

3.4.5. IRAS 23033+5951

As shown in Fig. 3, IRAS 23033+5951 is deeply embedded in the center of the dense molecular clump. Outflows in this region are well studied by many authors (e.g., Beuther et al. 2002b; Reid & Matthews 2008). Reid & Matthews (2008) also presented high-resolution interferometric data and revealed two massive cores, one with a massive protostar and another with the signature of infall suggesting that it might be collapsing.

3.4.6. IRAS 23385+6053

In Fig. 3, IRAS 23385+6053 is located in the center of the dense molecular clump. The IRAS source is associated with a powerful bipolar outflow seen in HCO^+ and SiO emission (Molinari et al. 1998b) and in CO J=2-1 (Wu et al. 2005; Zhang et al. 2005). However, the most compact VLA configuration revealed the existence of two nearby extended radio sources (Molinari et al. 2002), but no near infrared source is detected at the position of the IRAS source (Thompson & Macdonald 2003). Based on the physical and chemical nature of IRAS 23385+6053, Thompson & Macdonald (2003) concluded that the IRAS source is prior to the hot molecular core stage.

4. DISCUSSION

4.1. Luminosity to mass ratio

The ratio of infrared luminosity to molecular mass is roughly proportional to the star formation rate per unit mass, and could be a good indicator for star formation processes. To investigate the evolution of MSFRs, we compare the infrared luminosity to mass ratios of dense molecular clumps among different subgroups in our sample. In general, there is a trend that more luminous sources have higher $L_{\text{IR}}/M_{\text{VIR}}$ ratios as shown in Figure 4(left). A natural explanation for different $L_{\text{IR}}/M_{\text{VIR}}$ ratios is that the sources with lower ratios are younger since they are at the earlier evolutionary stage and have not yet reached their full luminosities (Sridharan et al. 2002). Usually, most massive stars are formed in most luminous clusters, and the massive stars dominate the luminosity of the clusters according to the mass-to-luminosity relation for zero age main sequence stars, $L \propto M^{3.5}$, and the IMF in the cluster (Kroupa 2001). Therefore, the $L_{\text{IR}}/M_{\text{VIR}}$ ratios might be an ambiguous indicator of the evolution of MSFRs: both massive stars formed in the cluster and late evolutionary stage of MSFR can lead to high ratios. Faúndez et al. (2004) argued that the $L_{\text{IR}}/M_{\text{VIR}}$ ratio could be interpreted as an indicator of which type of most massive star formed in the clump rather than an evolutionary effect.

To better understand the $L_{\text{IR}}/M_{\text{VIR}}$ ratio, we divided our sample into five subgroups in §3.3.5 and list their median values in Table 5. The median $L_{\text{IR}}/M_{\text{VIR}}$ ratios are 18, 28, 110 and 310 L_{\odot}/M_{\odot} for the subgroups **Low**, **HMPO**, **Control** and **Extreme**, respectively. The ratios among **Low**, **Control** and **Extreme** sources increase with their luminosities, which can most likely be interpreted as an indicator of which type of most massive star formed in the cluster. However, the **HMPO** sources have much lower $L_{\text{IR}}/M_{\text{VIR}}$ ratios than the **Control** ones, which is clearly seen Figure 4(left). This can not be interpreted by the type of massive star formed in the cluster since both types of sources share a similar luminosity range. Indeed, the **HMPO** sources are still deeply embedded in the dense clumps with much higher molecular masses compared to the **Control** ones (see the middle panel of Figure 4). Half of the latter sources are not associated with dense molecular clumps. We conclude that the **HMPO** sources are in an early evolutionary stage when the massive protostars have not reached their full luminosities of the zero-age main sequence stars and are still accreting material, supported by signatures of infall motions seen in about half of the **HMPO** sources (see the details in §3.4). Giannetti et al. (2017) proposed that the L_{IR}/M ratio is directly related with the gas temperature of molecular gas in a simple toy model of a spherical, internally heated clump, and the gas temperature is an indicator

of the evolutionary stage of the clump. They also pointed out that most HMPOs have L_{IR}/M ratios from $10 L_{\odot}/M_{\odot}$ to $\leq 40 L_{\odot}/M_{\odot}$, which is consistent with the values of more than half identified HMPOs in our paper.

We also compare our sample to a subsample with potential molecular outflows in the RMS survey (Lumsden et al. 2013; Maud et al. 2015a). Figure 4 shows the HMPOs (named MYSOs in Maud et al. 2015a) have slightly higher $L_{\text{IR}}/M_{\text{VIR}}$ ratios than the compact HII regions in the RMS sample. It also happens to the HMPOs and HII regions in the ATLASGAL survey (Urquhart et al. 2014). As Maud et al. (2015a) pointed out, this may be due to the fact that the HMPOs and compact HII regions are belonging to a similar evolutionary stage. However, the typical $L_{\text{IR}}/M_{\text{VIR}}$ values of HMPOs in the RMS sample are about two times as those in our sample. This may be due to a systematic change on calculating the gas masses with different tracers at different angular resolutions. The control sample in our paper includes much evolved sources, leading to this sample with high $L_{\text{IR}}/M_{\text{VIR}}$ ratios.

4.2. Implication on massive star formation

Having determined the physical properties of molecular clumps in MSFRs, we can investigate the massive star formation process with the derived parameters. The **HMPO** sources have the largest sizes and the **Low** have the smallest ones. The line widths have large variance and the median values are 1.74, 3.00, 1.91 and 3.55 km s^{-1} for the subgroups **Low**, **HMPO**, **Control** and **Extreme**, respectively. Figure 4(right) presents linewidth against FIR luminosity for our sample. The linewidth is an indicator of turbulent motion of the clumps associated with the IRAS sources. In general more luminous sources tend to be associated with clumps with broader line widths, but the scatter is large. Comparing the two subgroups **HMPO** and **Control**, one can find that the former has a much broader linewidth than the latter. The median linewidth of the **Extreme** sources is the broadest one among all subgroups (see Table 5).

To investigate the impact of the feedback from MSFRs, we compare our results with the outflow study by Zhang et al. (2005). Table 5 lists basic outflow parameters determined from Zhang’s sample with a similar FIR luminosity range as the subgroup **High**. We find that the typical kinetic energy of the outflows is about half of the kinetic energy of dense clumps of the **High** sources and one sixth of the **HMPO** sources, and the outflow timescale is one fourth of the dynamical values of the **High** and **HMPO** sources. It supports that the feedback (e.g., outflows) from MSFRs can play an important role on the surrounding environments. The variance of kinetic energies of different subgroups is quite large. The **Low** sources have the lowest kinetic energies since they only form low/intermediate mass stars. Both **HMPO** and **Control** sources are forming massive stars. However, the **Control** sources may have finished their mass accretion process, and their central protostars have reached their zero-age main sequence stages with full luminosities and strong UV radiation, ionizing and destroying the surrounding molecular clouds. If no continuous energy supply, kinetic energy in molecular clumps will dissipate as the sources evolve with time, and this may result in narrower linewidths at the later stage as seen in the **Control** sources. The newly formed massive stars in the **Extreme** sources have destroyed their natal clumps and the large linewidths might be due to the strong stellar wind from the central massive stars. The **HMPO** sources are still in a relatively early evolutionary stage when they are deeply embedded in the dense clumps with weak radio emission from the central protostars confined in small regions. Their central protostars have high mass accretion rate and are ejecting large amount of kinetic energy into the surrounding material through jets and outflows. Their feedbacks are very important to maintain the turbulent motion in the clumps as the median kinetic energy ratio of the outflows to the clumps ranges from 40% to 70% if considering the different timescales. Based on a much large outflow sample identified in the ATLASGAL survey, Yang et al. (2018) also find that outflow energy is comparable to the turbulent energy within the clump. It seems to support that turbulence in the **HMPO** sources may be largely supplied by the feedbacks from MSFRs. However, they find no evidence that outflows contribute significantly to the turbulent kinetic energy of surrounding materials. This is also confirmed by another work in a follow-up study of the RMS survey (Maud et al. 2015b). It suggests alternative means or undetected outflows may be responsible for the turbulence in the clumps.

5. CONCLUSION

We have mapped 39 massive star forming regions around the cold IRAS sources with high-velocity CO flows in CS $J=2 \rightarrow 1$. All sources are detected in CS $J=2 \rightarrow 1$, showing the existence of CS clumps around the IRAS sources. We have identified 12 high-mass protostellar object (HMPO) candidates in this sample. The HMPO candidates are characterized by low FIR luminosity to virial mass ratio because they are at very early evolutionary stages of star formation when the massive protostars have not reached their full luminosities of the zero-age main sequence stars.

Large turbulent motion in the HMPO sources may be largely due to the large kinetic energy ejected by the central protostars formed in dense clumps. However, alternative means or undetected outflows may also be responsible for the turbulence in the clumps.

We thank the anonymous referee for valuable comments that improved this manuscript. We are grateful for supporting by the staff of Nobeyama Radio Observatory, Japan. Y.A. acknowledges partial support by NSFC grant 11373007.

REFERENCES

- Ao, Y., Yang, J., & Sunada, K. 2004, *AJ*, 128, 1716
- Beuther, H., Schilke, P., Menten, K. M., et al. 2002a, *ApJ*, 566, 945
- Beuther, H., Schilke, P., Sridharan, T. K., et al. 2002b, *A&A*, 383, 892
- Blitz, L., Fich, M., & Stark, A. A. 1982, *ApJS*, 49, 183
- Brand, J., Cesaroni, R., Palla, F., & Molinari, S. 2001, *A&A*, 370, 230
- Bronfman, L., Nyman, L.-A., & May, J. 1996, *A&AS*, 115, 81
- Carpenter, J. M., Heyer, M. H., & Snell, R. L. 2000, *ApJS*, 130, 381
- Casoli, F., Dupraz, C., Gerin, M., Combes, F., & Boulanger, F. 1986, *A&A*, 169, 281
- Cesaroni, R., Felli, M., & Walmsley, C. M. 1999, *A&AS*, 136, 333
- Chavarría, L. A., Allen, L. E., Hora, J. L., Brunt, C. M., & Fazio, G. G. 2008, *ApJ*, 682, 445
- Churchwell, E. 2002, *ARA&A*, 40, 27
- Condon, J. J., Cotton, W. D., Greisen, E. W., et al. 1998, *AJ*, 115, 1693
- Cooper, H. D. B., Lumsden, S. L., Oudmaijer, R. D., et al. 2013, *MNRAS*, 430, 1125
- Csengeri, T., Bontemps, S., Wyrowski, F., et al. 2017, *A&A*, 601, A60
- Csengeri, T., Leurini, S., Wyrowski, F., et al. 2016a, *A&A*, 586, A149
- Csengeri, T., Weiss, A., Wyrowski, F., et al. 2016b, *A&A*, 585, A104
- Cyganowski, C. J., Brogan, C. L., & Hunter, T. R. 2007, *AJ*, 134, 346
- Elia, D., Molinari, S., Schisano, E., et al. 2017, *MNRAS*, 471, 100
- Elitzur, M., Hollenbach, D. J., & McKee, C. F. 1989, *ApJ*, 346, 983
- Esteban, C., López-Martín, L., López-Sánchez, Á. R., Cedrés, B., & García-Rojas, J. 2004, *PASP*, 116, 723
- Evans, N. J., II, & Blair, G. N. 1981, *ApJ*, 246, 394
- Faúndez, S., Bronfman, L., Garay, G., et al. 2004, *A&A*, 426, 97
- Fich, M., Blitz, L., & Stark, A. A. 1989, *ApJ*, 342, 272
- Fontani, F., Beltrán, M. T., Brand, J., et al. 2005, *A&A*, 432, 921
- Garay, G., & Lizano, S. 1999, *PASP*, 111, 1049
- Giannetti, A., Leurini, S., Wyrowski, F., et al. 2017, *A&A*, 603, A33
- Goddi, C., Moscadelli, L., Alef, W., et al. 2005, *A&A*, 432, 161
- Hosokawa, T., & Omukai, K. 2009, *ApJ*, 691, 823
- Hosokawa, T., Yorke, H. W., & Omukai, K. 2010, *ApJ*, 721, 478
- Hunter, T. R., Churchwell, E., Watson, C., et al. 2000, *AJ*, 119, 2711
- Juvela, M. 1996, *A&AS*, 118, 191
- Keto, E. 2007, *ApJ*, 666, 976
- Klaassen, P. D., & Wilson, C. D. 2007, *ApJ*, 663, 1092
- Klein, R., Posselt, B., Schreyer, K., Forbrich, J., & Henning, T. 2005, *ApJS*, 161, 361
- Kroupa, P. 2001, *MNRAS*, 322, 231
- Kurtz, S., Churchwell, E., & Wood, D. O. S. 1994, *ApJS*, 91, 659
- Li, G.-X., Urquhart, J. S., Leurini, S., et al. 2016, *A&A*, 591, A5
- Lumsden, S. L., Hoare, M. G., Urquhart, J. S., et al. 2013, *ApJS*, 208, 11
- Marín-Franch, A., Herrero, A., Lenorzer, A., et al. 2009, *A&A*, 502, 559
- Maud, L. T., Lumsden, S. L., Moore, T. J. T., et al. 2015a, *MNRAS*, 452, 637
- Maud, L. T., Moore, T. J. T., Lumsden, S. L., et al. 2015b, *MNRAS*, 453, 645
- McKee, C. F., & Tan, J. C. 2003, *ApJ*, 585, 850
- Minier, V., Burton, M. G., Hill, T., et al. 2005, *A&A*, 429, 945
- Miralles, M. P., Salas, L., Cruz-González, I., & Kurtz, S. 1997, *ApJ*, 488, 749
- Molinari, S., Brand, J., Cesaroni, R., Palla, F., & Palumbo, G. G. C. 1998a, *A&A*, 336, 339
- Molinari, S., Testi, L., Brand, J., Cesaroni, R., & Palla, F. 1998b, *ApJL*, 505, L39

- Molinari, S., Testi, L., Rodríguez, L. F., & Zhang, Q. 2002, *ApJ*, 570, 758
- Moscadelli, L., Cesaroni, R., & Rioja, M. J. 2005, *A&A*, 438, 889
- Moscadelli, L., Reid, M. J., Menten, K. M., et al. 2009, *ApJ*, 693, 406
- Mottram, J. C., Hoare, M. G., Lumsden, S. L., et al. 2010, *A&A*, 510, A89
- Mottram, J. C., Hoare, M. G., Lumsden, S. L., et al. 2007, *A&A*, 476, 1019
- Mottram, J. C., Hoare, M. G., Davies, B., et al. 2011, *ApJL*, 730, L33
- Narayanan, G., & Walker, C. K. 1996, *ApJ*, 466, 844
- Niwa, T., Tachihara, K., Itoh, Y., et al. 2009, *A&A*, 500, 1119
- Palumbo, G. G. C., Scappini, F., Pareschi, G., et al. 1994, *MNRAS*, 266, 123
- Pan, L., & Padoan, P. 2009, *ApJ*, 692, 594
- Panagia, N. 1973, *AJ*, 78, 929
- Pirogov, L., Zinchenko, I., Caselli, P., Johansson, L. E. B., & Myers, P. C. 2003, *A&A*, 405, 639
- Planck Collaboration, Ade, P. A. R., Aghanim, N., et al. 2016, *A&A*, 594, A26
- Plume, R., Jaffe, D. T., Evans, N. J., II, Martín-Pintado, J., & Gómez-González, J. 1997, *ApJ*, 476, 730
- Plume, R., Jaffe, D. T., & Evans, N. J., II 1992, *ApJS*, 78, 505
- Reid, M. J., Menten, K. M., Zheng, X. W., et al. 2009, *ApJ*, 700, 137
- Reid, M. A., & Matthews, B. C. 2008, *ApJ*, 675, 1343
- Russeil, D., Adami, C., & Georgelin, Y. M. 2007, *A&A*, 470, 161
- Rygl, K. L. J., Wyrowski, F., Schuller, F., & Menten, K. M. 2010, *A&A*, 515, A42
- Schaller, G., Schaerer, D., Meynet, G., & Maeder, A. 1992, *A&AS*, 96, 269
- Schnee, S., & Carpenter, J. M. 2009, *ApJ*, 698, 1456
- Schuller, F., Menten, K. M., Contreras, Y., et al. 2009, *A&A*, 504, 415
- Shirley, Y. L., Evans, N. J., II, Young, K. E., Knez, C., & Jaffe, D. T. 2003, *ApJS*, 149, 375
- Sridharan, T. K., Beuther, H., Schilke, P., Menten, K. M., & Wyrowski, F. 2002, *ApJ*, 566, 931
- Sunada, K., Nakazato, T., Ikeda, N., et al. 2007, *PASJ*, 59, 1185
- Sunada, K., Yamaguchi, C., Nakai, N., et al. 2000, *Proc. SPIE*, 4015, 237
- Tackenberg, J., Beuther, H., Henning, T., et al. 2012, *A&A*, 540, A113
- Tang, X. D., Henkel, C., Wyrowski, F., et al. 2018, *A&A*, 611, A6
- Tapia, M., Persi, P., Bohigas, J., & Ferrari-Toniolo, M. 1997, *AJ*, 113, 1769
- Thompson, M. A., & Macdonald, G. H. 2003, *A&A*, 407, 237
- Torrelles, J. M., Patel, N. A., Anglada, G., et al. 2003, *ApJL*, 598, L115
- Urquhart, J. S., Busfield, A. L., Hoare, M. G., et al. 2007a, *A&A*, 461, 11
- Urquhart, J. S., Busfield, A. L., Hoare, M. G., et al. 2008, *A&A*, 487, 253
- Urquhart, J. S., Busfield, A. L., Hoare, M. G., et al. 2007b, *A&A*, 474, 891
- Urquhart, J. S., Figura, C. C., Moore, T. J. T., et al. 2015, *MNRAS*, 452, 4029
- Urquhart, J. S., Figura, C. C., Moore, T. J. T., et al. 2014a, *MNRAS*, 437, 1791
- Urquhart, J. S., Hoare, M. G., Lumsden, S. L., et al. 2009a, *A&A*, 507, 795
- Urquhart, J. S., Hoare, M. G., Lumsden, S. L., et al. 2012, *MNRAS*, 420, 1656
- Urquhart, J. S., Hoare, M. G., Purcell, C. R., et al. 2009b, *A&A*, 501, 539
- Urquhart, J. S., König, C., Giannetti, A., et al. 2018, *MNRAS*, 473, 1059
- Urquhart, J. S., Moore, T. J. T., Csengeri, T., et al. 2014b, *MNRAS*, 443, 1555
- Urquhart, J. S., Moore, T. J. T., Hoare, M. G., et al. 2011a, *MNRAS*, 410, 1237
- Urquhart, J. S., Moore, T. J. T., Schuller, F., et al. 2013a, *MNRAS*, 431, 1752
- Urquhart, J. S., Morgan, L. K., Figura, C. C., et al. 2011b, *MNRAS*, 418, 1689
- Urquhart, J. S., Thompson, M. A., Moore, T. J. T., et al. 2013b, *MNRAS*, 435, 400
- Wienen, M., Wyrowski, F., Menten, K. M., et al. 2015, *A&A*, 579, A91
- Wienen, M., Wyrowski, F., Schuller, F., et al. 2012, *A&A*, 544, A146
- Williams, S. J., Fuller, G. A., & Sridharan, T. K. 2004, *A&A*, 417, 115
- Wood, D. O. S., & Churchwell, E. 1989, *ApJ*, 340, 265
- Wouterloot, J. G. A., Brand, J., & Fiegle, K. 1993, *A&AS*, 98, 589
- Wu, J., & Evans, N. J., II 2003, *ApJL*, 592, L79
- Wu, J., Evans, N. J., II, Shirley, Y. L., & Knez, C. 2010, *ApJS*, 188, 313
- Wu, Y., Zhang, Q., Chen, H., et al. 2005, *AJ*, 129, 330

- Wyrowski, F., Hofner, P., Schilke, P., et al. 1997, *A&A*, 320, L17
- Wyrowski, F., Schilke, P., Walmsley, C. M., & Menten, K. M. 1999, *ApJL*, 514, L43
- Xu, Y., Reid, M. J., Zheng, X. W., & Menten, K. M. 2006, *Science*, 311, 54
- Xu, Y., Shen, Z.-Q., Yang, J., et al. 2006, *AJ*, 132, 20
- Yang, A. Y., Thompson, M. A., Urquhart, J. S., & Tian, W. W. 2018, *ApJS*, 235, 3
- Yang, J., Jiang, Z., Wang, M., Ju, B., & Wang, H. 2002, *ApJS*, 141, 157
- Zapata, L. A., Rodríguez-Garza, C., Rodríguez, L. F., Girart, J. M., & Chen, H.-R. 2011, *ApJL*, 740, L19
- Zhang, B., Zheng, X. W., Reid, M. J., et al. 2009, *ApJ*, 693, 419
- Zhang, Q., Hunter, T. R., Brand, J., et al. 2005, *ApJ*, 625, 864
- Zinchenko, I., Forsstroem, V., Lapinov, A., & Mattila, K. 1994, *A&A*, 288, 601
- Zinchenko, I., Mattila, K., & Toriseva, M. 1995, *A&AS*, 111, 95
- Zinchenko, I., Pirogov, L., & Toriseva, M. 1998, *A&AS*, 133, 337

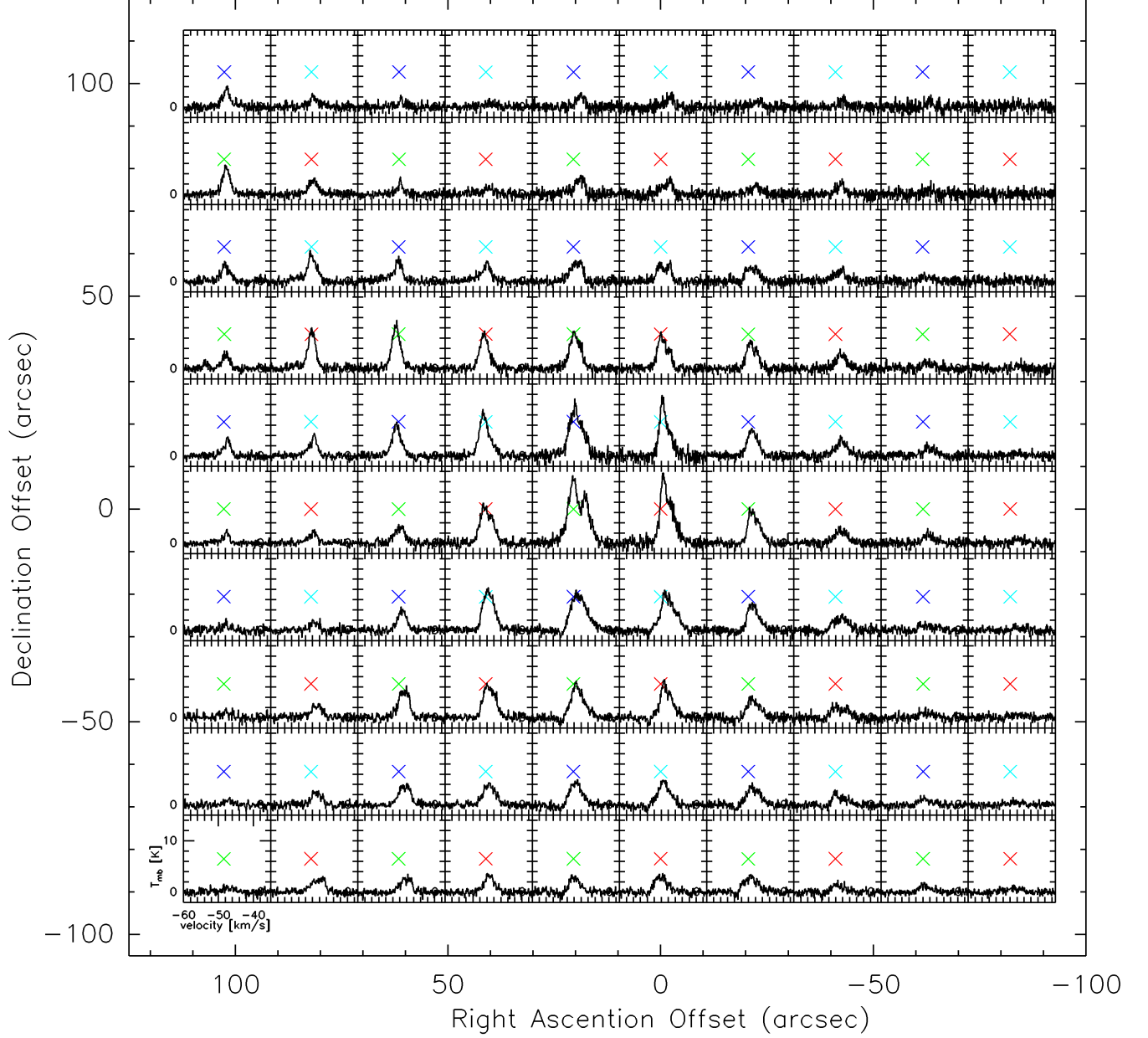


Figure 1. Mapping positions and profile map towards IRAS 02232+6138. The spectra marked by the crosses with the same color are taken from one snapshot observation, providing 25 spectra by the BEARS simultaneously. In total, four snapshot observations and 100 spectra are obtained for this target. The offsets are relative to the coordinate in Table 1.

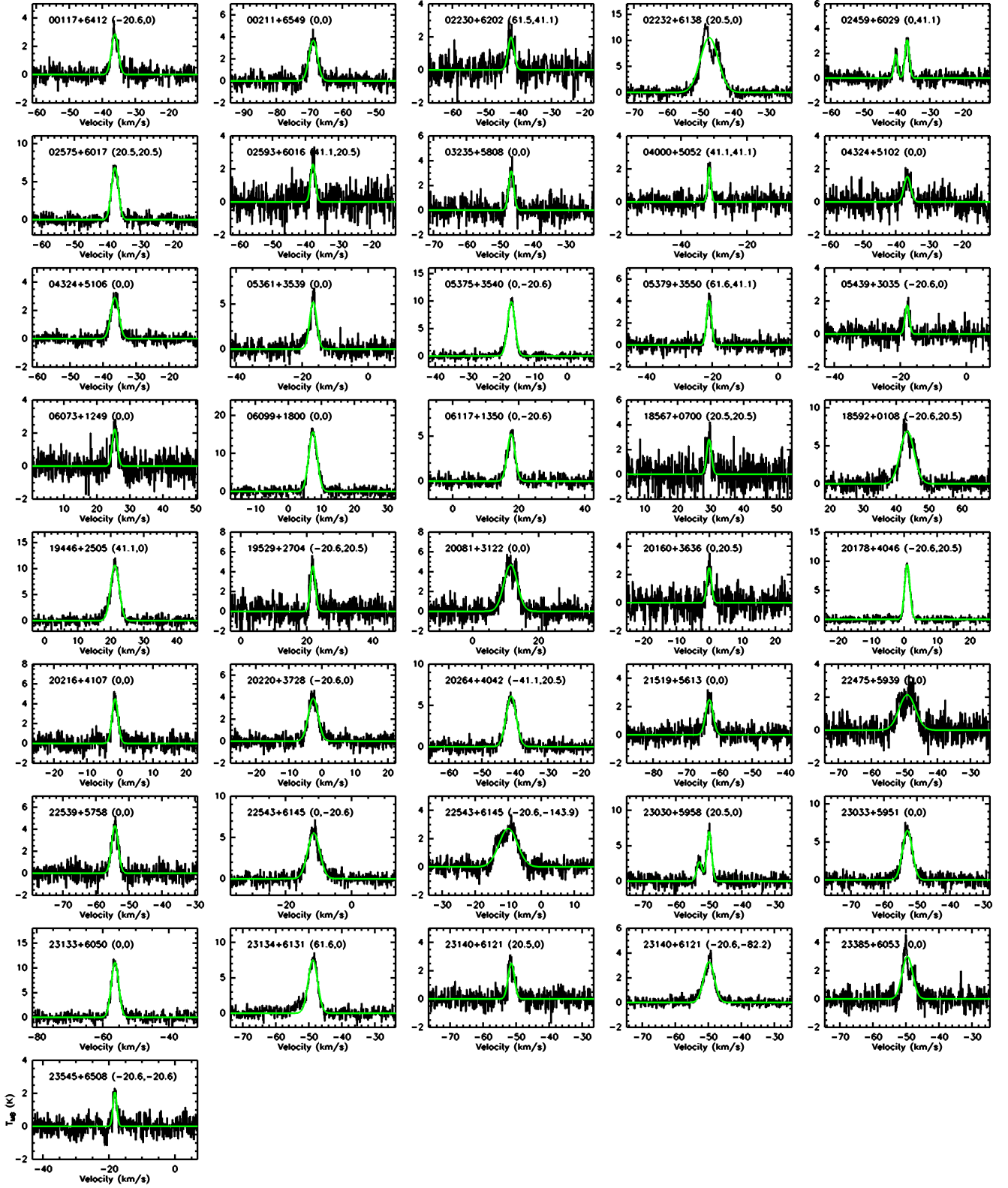


Figure 2. Spectra of the peak positions of clumps closed to the IRAS sources.

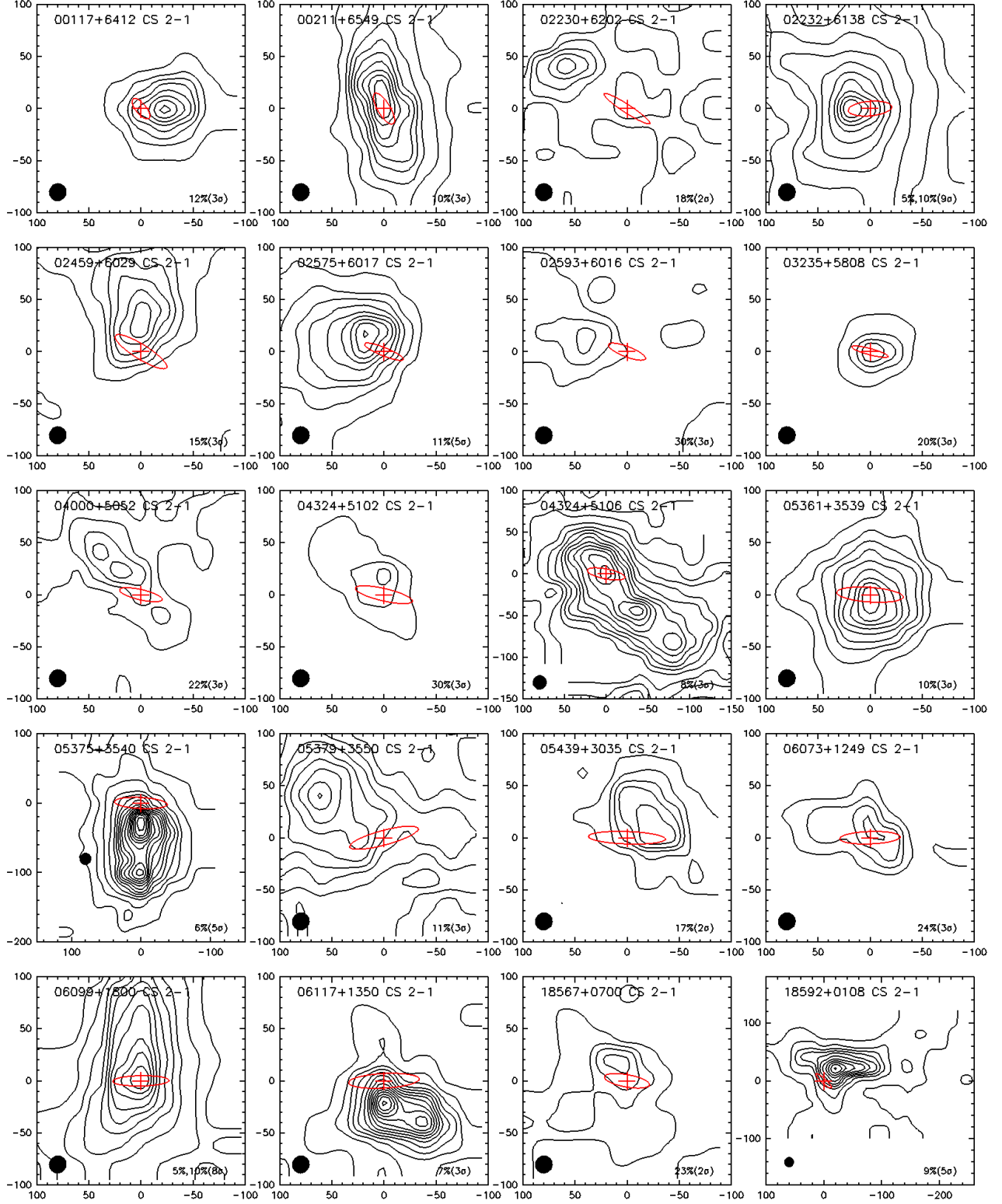


Figure 3. Contour maps of CS $J=2 \rightarrow 1$ integrated intensity. The source name and half power beam of NRO45m are given in the upper and lower-left of each panel. The contour level is given at the lower-right of each panel. For instance, "5%,10%(9 σ)" means the first contour is 5% of the peak intensity, the next contour is 10% of the peak intensity, and the interval is 10% or 9 σ . The positions and the error ellipse of IRAS sources are also marked with plus sign and ellipse. The positions of IRAS point sources are at (0,0).

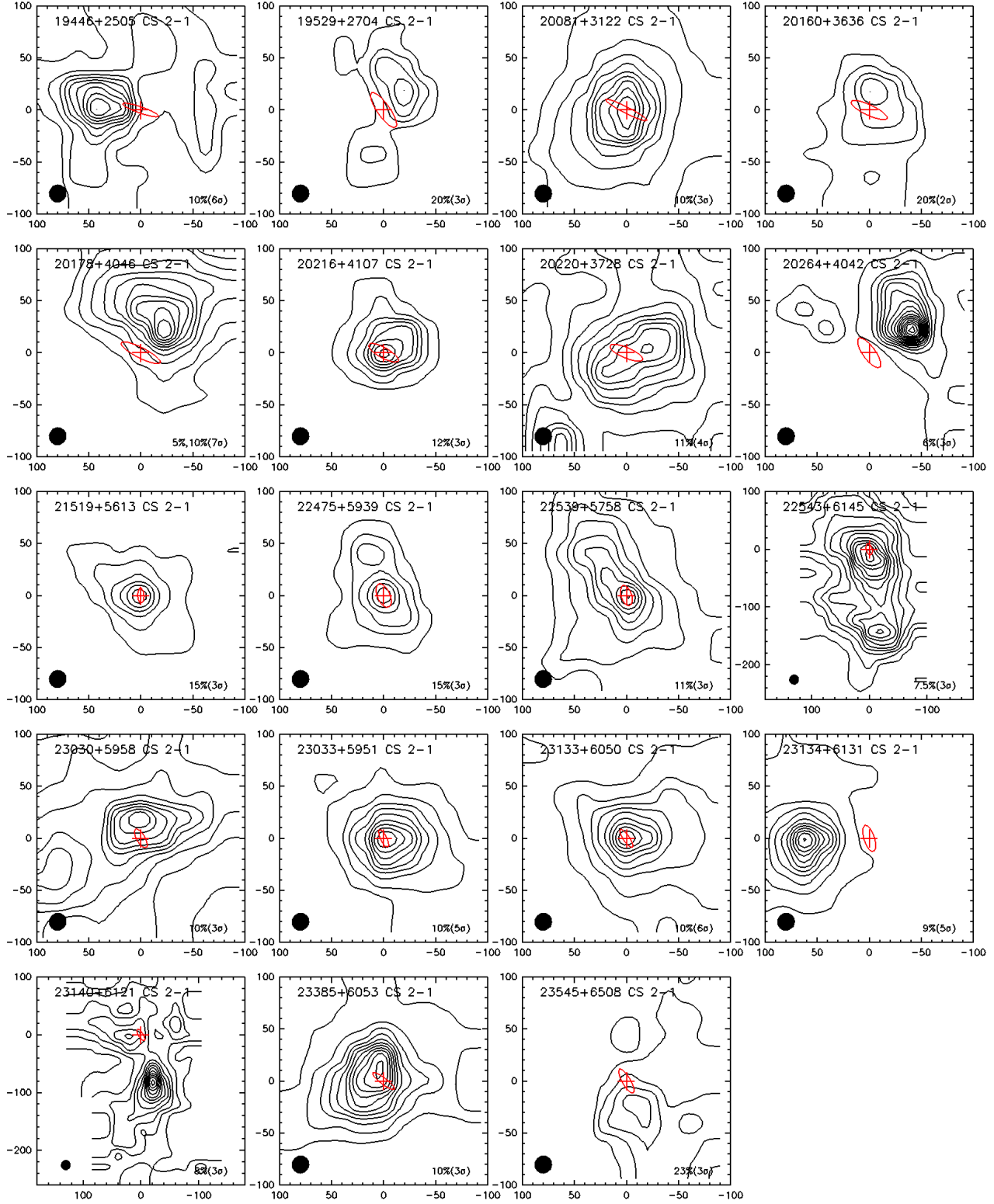


Figure 3. continued.

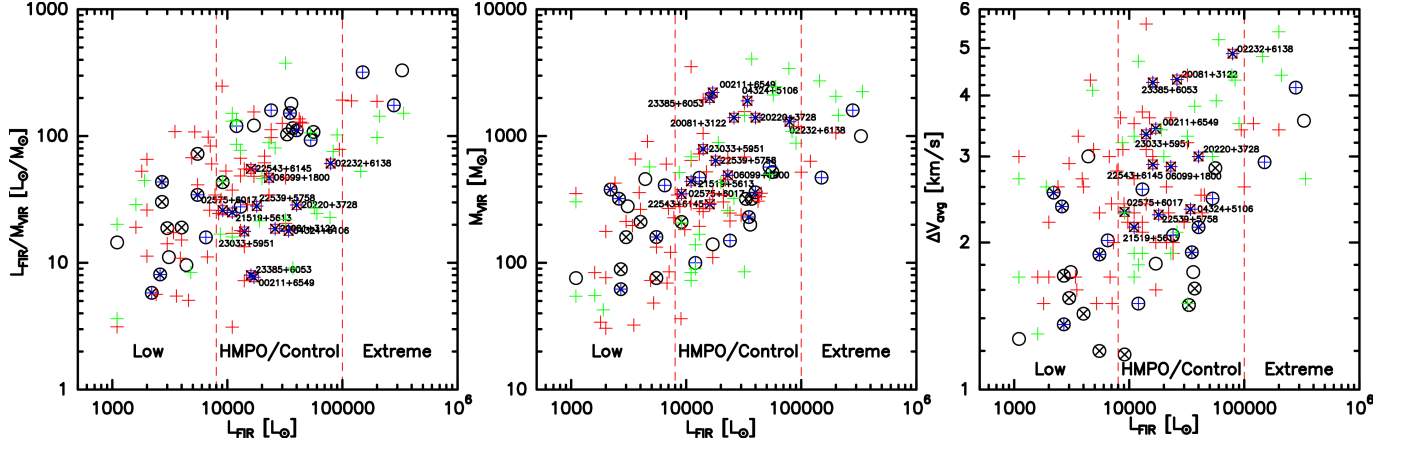


Figure 4. Luminosity plotted against Luminosity-to-mass ratio (**left panel**), virial mass (**middle panel**), and line width (**right panel**). The sources with cross symbols are deeply embedded in the dense clumps, and the ones with blue plus symbols associated with water masers. The red squares denote HMPO candidates and the open circles are the remaining sources. The YSOs and HII regions in Maud et al. (2015a), where the virial masses are derived from C^{18}O ($J=3\rightarrow 2$) data, are also presented as red and green plus signs, respectively. Vertical dashed lines in red represents the luminosities of $\sim 8 \times 10^3 L_{\odot}$ (above this threshold, the dense clumps will form massive stars) and $1.0 \times 10^5 L_{\odot}$.

Table 1. The source list

IRAS Name	RA	Dec.	L_{IR}	Dist.	Dist.	Comment ^a
	(J2000.0)	(J2000.0)	(L_{\odot})	(kpc)	ref.	
00117+6412	00:14:27.7	+64:28:46	2.2E+03	2.57±0.25	1	kinematic distance
00211+6549	00:23:58.0	+66:06:03	1.7E+04	5.60±0.33	1	kinematic distance
02230+6202	02:26:50.8	+62:15:52	2.4E+04	1.95±0.04	2	parallax measurement
02232+6138	02:27:01.0	+61:52:13	7.9E+04	1.95±0.04	2	parallax measurement
02459+6029	02:49:47.6	+60:42:07	3.0E+03	1.95±0.04	2	parallax measurement
02575+6017	03:01:29.2	+60:29:12	9.1E+03	1.95±0.04	2	parallax measurement
02593+6016	03:03:17.8	+60:27:52	1.2E+04	1.95±0.04	2	parallax measurement
03235+5808	03:27:31.1	+58:19:21	2.7E+03	1.95±0.04	2	parallax measurement
04000+5052	04:03:49.3	+51:00:48	1.1E+03	1.5 ^b	3	photometric distance
04324+5102	04:36:16.0	+51:08:12	9.1E+03	6.0±0.6	4	photometric distance
04324+5106	04:36:19.6	+51:12:44	3.4E+04	6.0±0.6	4	photometric distance
05361+3539	05:39:27.6	+35:40:42	2.6E+03	1.8 ^b	5	photometric distance
05375+3540	05:40:53.6	+35:42:15	1.3E+04	1.8 ^b	5	photometric distance
05379+3550	05:41:20.5	+35:52:06	3.1E+03	1.8 ^b	5	photometric distance
05439+3035	05:47:12.8	+30:36:11	4.0E+03	3.5±0.5	6	photometric distance
06073+1249	06:10:12.4	+12:48:45	3.3E+04	4.69 ^{+0.95} _{-0.83}	1	kinematic distance
06099+1800	06:12:53.3	+17:59:22	2.3E+04	1.59 ^{+0.07} _{-0.06}	7	parallax measurement
06117+1350	06:14:36.5	+13:49:35	5.3E+04	3.8±1.0	4	photometric distance
18567+0700	18:59:13.5	+07:04:47	5.5E+03	2.09±0.18	1	near kinematic distance
18592+0108	19:01:46.9	+01:13:07	2.8E+05	3.27 ^{+0.56} _{-0.42}	8	parallax measurement
19446+2505	19:46:47.0	+25:12:43	1.5E+05	2.5±0.4	9	photometric distance
19529+2704	19:54:59.6	+27:12:52	3.6E+04	3.2±1.1	10	photometric distance
20081+3122	20:10:09.1	+31:31:34	2.6E+04	2.57 ^{+0.34} _{-0.27}	7	parallax measurement
20160+3636	20:17:56.1	+36:45:33	3.7E+04	4.4±1.4	4	photometric distance
20178+4046	20:19:39.2	+40:56:30	1.7E+04	1.68±1.32	1	kinematic distance
20216+4107	20:23:23.8	+41:17:39	5.5E+03	2.35±0.77	1	far kinematic distance
20220+3728	20:23:55.6	+37:38:10	4.0E+04	3.68±0.47	1	far kinematic distance
20264+4042	20:28:12.4	+40:52:27	3.3E+05	7.09±0.27	1	kinematic distance
21519+5613	21:53:39.2	+56:27:45	1.1E+04	6.01±0.28	1	kinematic distance
22475+5939	22:49:29.4	+59:54:56	4.0E+04	4.11±0.27	1	kinematic distance
22539+5758	22:56:00.0	+58:14:45	1.8E+04	4.56±0.27	1	kinematic distance
22543+6145	22:56:19.1	+62:01:57	1.6E+04	0.70±0.04	11	parallax measurement
23030+5958	23:05:10.6	+60:14:40	3.5E+04	2.87±0.75	12	photometric distance
23033+5951	23:05:25.1	+60:08:11	1.4E+04	2.87±0.75	12	photometric distance
23133+6050	23:15:31.4	+61:07:09	5.6E+04	2.97±0.31	12	photometric distance
23134+6131	23:15:34.6	+61:47:42	4.4E+03	2.8±0.9	4	photometric distance
23140+6121	23:16:11.7	+61:37:44	6.5E+03	2.8±0.9	4	photometric distance
23385+6053	23:40:53.1	+61:10:21	1.6E+04	3.86±0.27	1	kinematic distance
23545+6508	23:57:05.2	+65:25:10	2.7E+03	1.14±0.24	1	kinematic distance

^a Kinematic distances are calculated using the revised prescription given in Reid et al. (2009). A near kinematic distance is adopted for 18567+0700 and far kinematic distances for 20216+4107 and 20220+3728.

^b For these sources, errors are not assigned in the literature.

References : (1) This work (2) Xu et al. (2006a); (3) Esteban et al. (2004); (4) Blitz & Fich (1982); (5) Evans & Blair (1981); (6) Tapia et al. (1997); (7) Rygl et al. (2010); (8) Zhang et al. (2009); (9) Marin-Franch et al. (2009); (10) Fich et al. (1989); (11) Moscadelli et al. (2009); (12) Russeil et al. (2007).

Table 2. Observational parameters of peak CS $J=2\rightarrow1$ spectra for IRAS sources

IRAS Name	$\Delta\alpha$ ($''$)	$\Delta\delta$ ($''$)	T_{mb} (K)	V_{LSR} (km s^{-1})	Line Width (km s^{-1})	$\int T_{\text{mb}} dv$ (K km s^{-1})
00117+6412	-20.6	0.0	3.05(40)	-36.2	2.44(12)	7.44(30)
00211+6549	0.0	0.0	3.93(49)	-68.8	3.03(13)	11.90(41)
02230+6202	61.5	41.1	2.11(58)	-42.2	2.15(22)	4.55(40)
02232+6138	20.5	0.0	11.22(64)	-47.2	6.41(8)	71.88(76)
02459+6029	0.0	41.1	3.30(38)	-36.8	1.52(8)	5.01(22)
	0.0	41.1	2.04(38)	-40.3	1.29(15)	2.64(22)
02575+6017	20.5	20.5	7.32(53)	-37.7	2.47(6)	18.07(39)
02593+6016	41.1	20.5	2.44(66)	-37.7	1.73(19)	4.23(40)
03235+5808	0.0	0.0	3.36(62)	-46.5	1.84(13)	6.18(39)
04000+5052	41.1	41.1	2.25(40)	-31.4	1.21(11)	2.72(21)
04324+5102	0.0	0.0	1.64(51)	-36.5	2.36(30)	3.88(39)
04324+5106	0.0	0.0	3.12(27)	-36.4	2.89(8)	9.01(22)
05361+3539	0.0	0.0	5.57(65)	-16.7	2.54(13)	14.16(54)
05375+3540	0.0	-20.6	10.52(44)	-17.0	2.64(4)	27.76(34)
05379+3550	61.6	41.1	4.30(43)	-21.0	1.73(8)	7.44(27)
05439+3035	-20.6	0.0	1.86(40)	-17.9	1.51(14)	2.82(23)
06073+1249	0.0	0.0	2.39(56)	25.5	1.80(18)	4.30(36)
06099+1800	0.0	0.0	16.65(81)	7.5	3.03(5)	50.37(67)
06117+1350	0.0	-20.6	5.55(44)	17.7	2.72(7)	15.10(34)
18567+0700	20.5	20.5	3.00(94)	29.6	1.68(26)	5.06(61)
18592+0108	-20.6	20.5	7.35(68)	43.4	4.97(11)	36.48(70)
19446+2505	41.1	0.0	11.36(62)	21.3	3.06(6)	34.72(52)
19529+2704	-20.6	20.5	4.86(85)	21.9	1.76(13)	8.54(53)
20081+3122	0.0	0.0	5.00(72)	11.6	4.81(16)	24.05(72)
20160+3636	0.0	20.5	2.65(72)	-0.0	1.62(25)	4.31(48)
20178+4046	-20.6	20.5	10.05(41)	1.0	1.89(3)	19.03(26)
20216+4107	0.0	0.0	4.81(61)	-1.5	2.14(11)	10.29(43)
20220+3728	-20.6	0.0	4.14(44)	-2.6	3.55(12)	14.68(40)
20264+4042	-41.1	20.5	6.50(49)	-41.1	3.62(8)	23.57(43)
21519+5613	0.0	0.0	2.65(46)	-63.0	2.63(18)	6.97(37)
22475+5939	0.0	0.0	2.28(55)	-49.1	5.81(27)	13.24(59)
22539+5758	0.0	0.0	4.61(56)	-54.2	2.37(10)	10.93(40)
22543+6145	0.0	-20.6	5.89(52)	-11.5	4.32(11)	25.44(52)
22543+6145S	-20.6	-143.9	2.89(38)	-10.0	6.54(16)	18.89(44)
23030+5958	20.5	0.0	2.92(64)	-52.9	1.84(17)	5.36(43)
	20.5	0.0	7.47(64)	-49.9	1.76(7)	13.13(44)
23033+5951	0.0	0.0	6.94(60)	-52.9	3.51(10)	24.35(54)
23133+6050	0.0	0.0	11.84(69)	-56.3	2.67(5)	31.67(54)
23134+6131	61.6	0.0	8.00(61)	-48.7	3.35(9)	26.79(54)
23140+6121	20.5	0.0	2.69(47)	-51.5	2.26(15)	6.08(34)
23140+6121S	-20.6	-82.2	3.51(25)	-49.8	3.78(8)	13.23(23)
23385+6053	0.0	0.0	3.21(48)	-49.6	3.76(16)	12.04(44)
23545+6508	-20.6	-20.6	2.22(42)	-18.2	1.35(14)	2.99(24)

Table 3. Derived parameters of CS $J=2\rightarrow 1$ maps for IRAS sources

IRAS Name	R	$\overline{\Delta v}$	M_{VIR}	$L_{\text{IR}}/M_{\text{VIR}}$	Notes ^a
	(pc)	(km s ⁻¹)	(M_{\odot})	(L_{\odot}/M_{\odot})	
00117+6412	0.29	2.53	3.8E+02	5.8E+00	Y
00211+6549	0.91	3.42	2.2E+03	7.6E+00	Y
02230+6202	0.17	2.07	1.5E+02	1.6E+02	N
02232+6138	0.26	4.87	1.3E+03	6.0E+01	Y
02459+6029	0.33	1.54	1.6E+02	1.8E+01	Y
02575+6017	0.31	2.31	3.5E+02	2.6E+01	Y
02593+6016	0.21	1.50	1.0E+02	1.1E+02	N
03235+5808	0.15	1.71	8.9E+01	3.0E+01	Y
04000+5052	0.23	1.27	7.6E+01	1.5E+01	N
04324+5102	0.73	1.18	2.1E+02	7.8E+01	Y
04324+5106	1.66	2.34	1.9E+03	3.2E+01	Y
05361+3539	0.27	2.37	3.2E+02	8.0E+00	Y
05375+3540	0.34	2.57	4.7E+02	2.9E+01	N
05379+3550	0.44	1.74	2.8E+02	1.1E+01	N
05439+3035	0.49	1.43	2.1E+02	1.9E+01	Y
06073+1249	0.68	1.49	3.2E+02	1.0E+02	Y
06099+1800	0.29	2.86	4.9E+02	4.7E+01	Y
06117+1350	0.45	2.46	5.7E+02	9.3E+01	N
18567+0700	0.25	1.20	7.6E+01	7.2E+01	Y
18592+0108	0.45	4.15	1.6E+03	1.7E+02	N
19446+2505	0.26	2.92	4.7E+02	3.1E+02	N
19529+2704	0.32	1.74	2.0E+02	1.8E+02	N
20081+3122	0.37	4.31	1.4E+03	1.8E+01	Y
20160+3636	0.59	1.61	3.2E+02	1.2E+02	Y
20178+4046	0.21	1.81	1.4E+02	1.1E+02	N
20216+4107	0.22	1.89	1.6E+02	3.4E+01	Y
20220+3728	0.76	3.00	1.4E+03	2.8E+01	Y
20264+4042	0.39	3.55	1.0E+03	3.2E+02	N
21519+5613	0.46	2.15	4.4E+02	2.5E+01	Y
22475+5939	0.37	2.15	3.6E+02	1.1E+02	Y
22539+5758	0.59	2.28	6.4E+02	2.9E+01	Y
22543+6145	0.17	2.89	2.9E+02	5.3E+01	Y
23030+5958	0.30	1.91	2.3E+02	1.5E+02	Y
23033+5951	0.33	3.33	7.9E+02	1.8E+01	Y
23133+6050	0.33	2.84	5.2E+02	9.6E+01	Y
23134+6131	0.24	3.00	4.6E+02	9.5E+00	N
23140+6121	0.48	2.02	4.1E+02	1.6E+01	N
23385+6053	0.52	4.25	2.0E+03	8.4E+00	Y
23545+6508	0.16	1.36	6.2E+01	4.3E+01	Y

^a Y: an IRAS source, located within the contour level of 50% of the peak, is deeply embedded in the dense gas cloud; N: an IRAS source is not deeply embedded in the dense gas cloud.

Table 4. HMPO candidates in the sample

IRAS Name	FIR Properties			Radio Properties						
	L_{IR} (L_{\odot})	Mu^a (M_{\odot})	Spec. ^b Type	$S_{1.4\text{GHz}}^c$ (mJy)	$\log N'_c$ (s^{-1})	Spec. ^d Type	H_2O^e maser	Dense ^f Core	Massive ^g Star	HMPO Candidate
00117+6412	2.2E+03	5.5	>B3	$\leq 2.5\text{E}+00$	44.8	$\geq \text{B2}$	Y	Y	N	N
00211+6549	1.7E+04	10.1	B1	$\leq 2.5\text{E}+00$	45.5	$\geq \text{B1}$	Y	Y	Y	Y
02230+6202	2.4E+04	11.3	B1	1.1E+04	48.2	O8	Y	N	N	N
02232+6138	7.9E+04	16.7	B0	3.8E+01	45.7	B1	Y	Y	Y	Y
02459+6029	3.0E+03	6.0	>B3	$\leq 2.5\text{E}+00$	44.6	$\geq \text{B2}$	N	Y	N	N
02575+6017	9.1E+03	8.3	B2	$\leq 2.5\text{E}+00$	44.6	$\geq \text{B2}$	Y	Y	Y	Y
02593+6016	1.2E+04	8.9	B2	1.0E+03	47.2	B0	Y	N	N	N
03235+5808	2.7E+03	5.8	>B3	2.0E+01	45.5	B1	N	Y	N	N
04000+5052	1.1E+03	4.6	>B3	1.5E+01	45.1	B1	N	N	N	N
04324+5102	9.1E+03	8.3	B2	$\leq 2.5\text{E}+00$	45.5	$\geq \text{B1}$	N	Y	Y	N
04324+5106	3.4E+04	12.6	B0.5	2.0E+02	47.5	B0	Y	Y	Y	Y
05361+3539	2.6E+03	5.8	>B3	$\leq 2.5\text{E}+00$	44.5	$\geq \text{B2}$	Y	Y	N	N
05375+3540	1.3E+04	9.3	B2	2.5E+02	46.5	B0.5	Y	N	N	N
05379+3550	3.1E+03	6.0	B3	$\leq 2.5\text{E}+00$	44.5	$\geq \text{B2}$	N	N	N	N
05439+3035	4.0E+03	6.5	B3	$\leq 2.5\text{E}+00$	45.1	$\geq \text{B1}$	N	Y	N	N
06073+1249	3.3E+04	12.4	B0.5	3.5E+01	46.5	B0.5	N	Y	Y	N
06099+1800	2.3E+04	11.1	B1	$\leq 2.5\text{E}+00$	44.4	$\geq \text{B2}$	Y	Y	Y	Y
06117+1350	5.3E+04	14.7	B0.5	2.3E+01	46.1	B0.5	Y	N	N	N
18567+0700	5.5E+03	7.2	B3	$\leq 2.5\text{E}+00$	44.6	$\geq \text{B2}$	N	Y	N	N
18592+0108	2.8E+05	19.0	O9.5	1.0E+04	48.6	O8	Y	N	N	N
19446+2505	1.5E+05	18.2	B0	4.0E+03	48.0	O8.5	Y	N	N	N
19529+2704	3.6E+04	12.9	B0.5	1.8E+03	47.9	O9	N	N	N	N
20081+3122	2.6E+04	11.6	B1	3.4E+01	45.9	B0.5	Y	Y	Y	Y
20160+3636	3.7E+04	13.0	B0.5	4.5E+01	46.5	B0.5	N	Y	Y	N
20178+4046	1.7E+04	10.1	B1	2.8E+01	45.5	B1	N	N	N	N
20216+4107	5.5E+03	7.1	B3	$\leq 2.5\text{E}+00$	44.7	$\geq \text{B2}$	Y	Y	N	N
20220+3728	4.0E+04	13.3	B0.5	6.3E+02	47.5	B0	Y	Y	Y	Y
20264+4042	3.3E+05	19.1	O9.5	4.0E+03	48.9	O8	N	N	N	N
21519+5613	1.1E+04	8.8	B2	$\leq 2.5\text{E}+00$	45.5	$\geq \text{B1}$	Y	Y	Y	Y
22475+5939	4.0E+04	13.4	B0.5	2.3E+03	48.2	O8	Y	Y	Y	N
22539+5758	1.8E+04	10.3	B1	$\leq 2.5\text{E}+00$	45.3	$\geq \text{B1}$	Y	Y	Y	Y
22543+6145	1.6E+04	9.8	B1	5.9E+01	45.1	B1	Y	Y	Y	Y
23030+5958	3.5E+04	12.8	B0.5	1.9E+03	47.8	O9	Y	Y	Y	N
23033+5951	1.4E+04	9.6	B2	$\leq 2.5\text{E}+00$	44.9	$\geq \text{B2}$	Y	Y	Y	Y
23133+6050	5.6E+04	14.7	B0.5	7.1E+02	47.4	B0	N	Y	Y	N
23134+6131	4.4E+03	6.7	B3	$\leq 2.5\text{E}+00$	44.9	$\geq \text{B2}$	N	N	N	N
23140+6121	6.5E+03	7.5	B3	$\leq 2.5\text{E}+00$	44.9	$\geq \text{B2}$	Y	N	N	N
23385+6053	1.6E+04	9.9	B1	7.2E+01	46.6	B0.5	Y	Y	Y	Y
23545+6508	2.7E+03	5.8	>B3	$\leq 2.5\text{E}+00$	44.1	$\geq \text{B3}$	Y	Y	N	N

The HMPO candidates are shown in bold font.

^a The mass of the most massive star formed in a cluster.

^b Spectral type is determined by the luminosity of the most massive star formed in a cluster (Panagia 1973).

^c A upper limit of 5σ is adopted for an undetected source.

^d Spectral type is determined by the number of photons of the Lyman continuum (Panagia 1973).

^e Association with a detected water maser (Sunada et al. 2007).

^f Same as in Table 3.

^g Whether the mass of the most massive star in a cluster is higher than $8 M_{\odot}$.

Table 5. Statistics of derived parameters for the subgroups of the sample

subgroup ^a	Count ^b	L_{FIR} (L_{\odot})	M_{VIR} (M_{\odot})	$L_{\text{IR}}/M_{\text{VIR}}$ (L_{\odot}/M_{\odot})	ΔV (km s^{-1})	R (pc)	t_{dyn}^c (yrs)	t_{ff}^c (yrs)	t_{msf}^c (yrs)	E_{kin}^c (ergs)
Low	12/ 8/ 5	3.1E+03	2.1E+02	1.8E+01	1.74	0.27	4.8E+05	2.1E+05	...	3.1E+45
HMPO	12/12/12	1.8E+04	1.0E+03	2.8E+01	3.00	0.46	3.6E+05	1.5E+05	2.0E+05	4.6E+46
Control	12/ 6/ 6	3.5E+04	3.2E+02	1.1E+02	1.91	0.34	4.6E+05	2.0E+05	...	4.4E+45
Extreme	3/ 0/ 2	2.8E+05	1.0E+03	3.1E+02	3.55	0.39	2.9E+05	1.2E+05	...	6.9E+46
High	27/18/20	2.6E+04	4.8E+02	7.8E+01	2.46	0.37	3.6E+05	1.5E+05	...	1.8E+46
Maud15a HMPOs ^d	31	1.7E+04	3.4E+02	5.3E+01	2.5	0.44				
Maud15a H II ^d	21	2.3E+04	5.0E+02	7.6E+01	3.2	0.47				
Zhang05 ^e	21	2.4E+04	8.3E+04	7.2E+45

^a The sample is divided into five subgroups (subgroups **Low**, **HMPO**, **Control**, **Extreme** and **High**, see details in § 3.3.5).

^b n1/n2/n3: n1 is the number of the sources in the subgroup, n2 the number of the sources associated with dense clumps and n3 the number of the sources with the detection of water masers.

^c See § 3.3.5 for the details of the calculations of timescales and energy. The star formation timescales are estimated only for the **HMPO** sources as their molecular clouds where the massive protostars are forming are not largely affected by the strong feedbacks of MSFRs.

^d The selected HMPOs and compact H II regions in the RMS survey (Maud et al. 2015a) have a luminosity range from 8×10^3 to $10^5 L_{\odot}$.

^e The median values (dynamical timescale and kinetic energy) of outflows for the subsample in Zhang et al. (2005). This subsample share the similar luminosity range as subgroup **High**.